Available online at www.sciencedirect.com

jmr&t Journal of Materials Research and Technology

journal homepage: www.elsevier.com/locate/jmrt

Original Article

Mixture optimisation for cement-soil mixtures with embedded GFRP tendons

Genbao Zhang [a,c], Changfu Chen [d,e], Junbo Sun [b,*], Kefei Li [f], Fan Xiao [g], Yufei Wang [h,**], Mengcheng Chen [i], Jizhuo Huang [j], Xiangyu Wang [h,***]

[a] College of Civil Engineering, Hunan City University, Yiyang, Hunan, 413000, PR China
[b] Institute for Smart City of Chongqing University in Liyang, Chongqing University, Jiangsu, 213300, China
[c] Hunan Engineering Research Center of Structural Safety and Disaster Prevention for Urban Underground Infrastructure, Yiyang, Hunan, 413000, PR China
[d] Key Laboratory of Building Safety and Energy Efficiency of the Ministry of Education, Hunan University, Changsha, Hunan 410082, PR China
[e] College of Civil Engineering, Hunan University, Changsha, Hunan, 410082, PR China
[f] School of Civil and Environmental Engineering, University of New South Wales, Sydney, NSW, 2052, Australia
[g] College of Management, Zhongkai University of Agriculture and Engineering, Guangzhou, 510225, China
[h] School of Design and Built Environment, Curtin University, Perth, WA, 6102, Australia
[i] School of Civil Engineering and Architecture, East China Jiao Tong University, Nanchang, 330013, China
[j] College of Civil Engineering, Fuzhou University, 2 Xue Yuan Rd., University Town, Fuzhou Province, 350116, China

ARTICLE INFO

Article history:
Received 2 November 2021
Accepted 15 February 2022
Available online 26 February 2022

Keywords:
Cemented soil
Interface bond strength
Glass fiber reinforced polymer reinforcement
Machine learning
Multi-objective optimisation

ABSTRACT

The glass fiber-reinforced polymer (GFRP) rebar reinforced cemented soil is widely employed to solve the weak foundation problem led by sludge particularly. The robustness of this structure is highly dependent on the interface bond strength between the GFRP tendon and cemented soils. However, its application is obstructed owing to the deficient studies on the influence factors. Therefore, this study investigates the effects of water content (C_w: 50%–90%), cement proportion (C_c: 6%–30%), and curing period (T_c: 28–90 days) on peak and residual interface bond strengths (T_p and T_t), as well as the unconfined compression strength (UCS). Results indicated that mechanical properties were positively responded to T_c and C_c, while negatively correlated to C_w. Besides, Random Forest (RF), one of the machine learning (ML) models, was developed with its hyperparameters tuned by the firefly algorithm (FA) based on the experimental dataset. The pullout strength was predicted by the ML model for the first time. High correlation coefficients and low root-mean-square errors verified the accuracy of established RF-FA models in this study. Subsequently, a coFA-based multi-objective optimisation firefly algorithm (MOFA) was introduced to optimise tri-objectives between UCS, T_p (or T_t), and cost. The Pareto fronts were successfully acquired for optimal mixture designs, which contributes to the application of GFRP tendon reinforced cemented soil in practice. In addition, the sensitivity of input variables was evaluated and ranked.

* Corresponding author.
** Corresponding author.
*** Corresponding author.
E-mail addresses: tunneltc@gmail.com (J. Sun), wangyf0113_suz@163.com (Y. Wang), Xiangyu.Wang@curtin.edu.au (X. Wang).

https://doi.org/10.1016/j.jmrt.2022.02.076

1. Introduction

Cement is extensively applied in foundation improvement and stabilisation to avoid sludge-induced problems particularly [1–4]. Cement-soil composite is generated from the pozzolanic activities caused by cement filling the pores in sludge using soil mixing technique. The characteristics of this mixed material are enhanced compared to that of the soil [4–6]. Some solid wastes are also investigated for concrete performance enhancement and sustainability, which have the potential to be used in soil [7–11]. However, only cement-soil composite alone is deficient to withstand the lateral earth pressure in foundation pit support and blocking surface water. The utilisation of steel rebar as part of the structure combined with cement-soil matrix is one safer way to sustain the exterior load [12–14]. However, the performance of the whole composite is inevitably degraded by the steel corrosion during its usage which has an especially serious impact on permanent structures [15–18]. In case of degradation, the glass fiber-reinforced polymer (GFRP) becomes a new tendon material to displace the steel for its excellent engineering characteristics and high affordability [19–23].

The interface bond performance of GFRP tendon-reinforced cemented soils (GTRCS) presents their pullout capability, in analogy to reinforced concrete [24–26]. In many circumstances, failures are induced by the bonding surface detachment but not the tendon reaching its ultimate strength. Although it is essential, the interface-bond-strength-related failure patterns are still indeterminate resulting in insufficient design codes of reinforced cement-soil structures [12,25]. Furthermore, preceding studies are mainly about cemented soil's mechanical and hydraulic capacities with few concerning the bond performance between soil and GFRP reinforcements [27–29]. These obstruct the application of GTRCS in practice. Therefore, the investigation related to the interface bonding strength of GTRCS is necessary.

To this end, some influencing factors are explored for the bonding strength of GTRCS. Cement-soil composite consists of cement, soil, and water with its mechanical properties being affected by them [30–32]. Thereby, water content (C_w), cement content (C_c), and curing time (T_c) are three variables in this study. However, the laboratory approach required vast effort to obtain reliable conclusions of these variables, including heavy workload and numerous investing resources. The subsequent result analysis conducted by regression functions was inadequate because researchers usually designed representative mixtures to conduct tests and conclude their findings [33,34]. To deal with this problem, investigators adopted machine learning models (ML) on the basis of their existing experiment dataset and explored corresponding inherent patterns [35–38]. Random forest (RF) as one of the widespread ML models, had excellent generalisation and calculation capacities in the information field. Furthermore, it also performed well in avoiding data overfitting and better tolerance for outliers as well as noise compared to other models like support vector regression (SVR) and artificial neural network (ANN) [39–41]. Hence, this model was adopted in the data analysis of the study.

However, the limitation for RF's high dependency on hyperparameters restricted its performances [42,43]. This difficulty of hyperparameters adjustment was dealt with optimisation algorithms by replacing conventional methodologies [44,45]. The firefly algorithm (FA) became the primary choice because of its characteristics for automatic subdivision and multimodality elimination among common algorithms, including the genetic algorithm (GA) and particle swarm optimisation (PSO) [46]. Therefore, researchers adopted this algorithm to adjust hyperparameters of the RF model (FA-RF). The aim of this study was to determine the desirable mixtures by overall considering performances and production cost of cemented soil mixtures. Accordingly, a multi-objective optimisation (MOO) model was proposed to fulfill this demand relying on a metaheuristic algorithm [47]. It enabled to propose Pareto solutions to achieve optimisations of various objectives with limits of nonlinear constraints. Zhang et al. [48] previously solved the optimising demands of slump, strength,

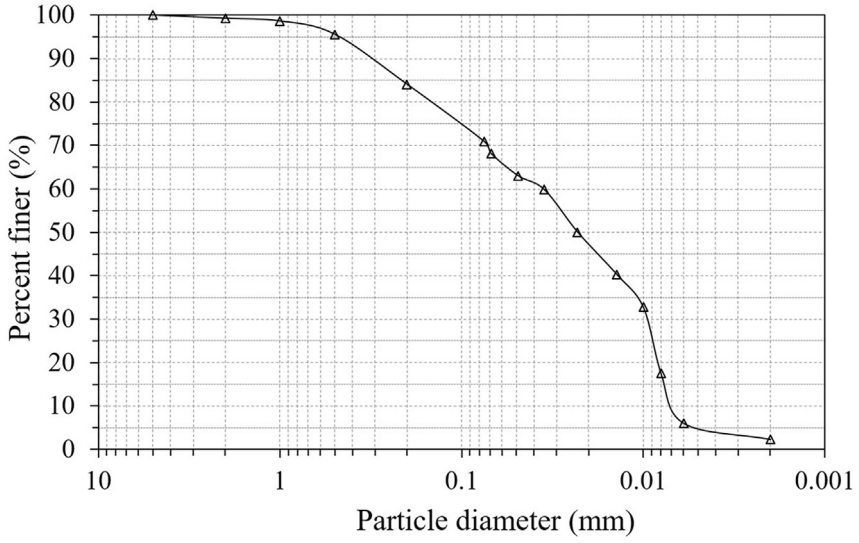

Fig. 1 – Detailed particle sizes of soil sample [50].

Table 1 – Materials used in the experimental program [50].

Properties	Values
Soil	
Specific gravity	2.705
Natural moisture content (%)	30–90
Liquid limit (%)	58.1
Plasticity limit (%)	28.6
Cement	
Type	P.O 42.5
Specific gravity (t/m^3)	3.0–3.2
Compressive strength (MPa)	≥42.5 (28-day)
Normal consistency (%)	27
GFRP reinforcement	
Type	GFRP tendon
Rib spacing (mm)	10.1
Tensile strength (MPa)	466
External diameter (mm)	16.8
Internal diameter (mm)	15
Young's modulus (GPa)	40

and cost of plastic concrete. Similarly, three objectives of GTRCS, including T_p, T_t and cost, were optimised by introducing MOO based on the FA-RF (MOFA-RF).

In this study, compressive and pullout strengths were carried out to investigate the impact of three variables (C_c, C_w, T_c) on GTRCS. The dataset consists of 150 groups of compressive and pullout strengths (peak and residual), as shown in the Appendix, which was then utilised for machine learning prediction for the first time. Subsequently, the MOFA-RF was established for tri-objective GTRCS optimisation mixture design through obtaining the Pareto fronts. Finally, ranking importance for input variables was explored.

2. Experimental programs

2.1. Materials

The soil was gathered from the floodplain at the confluence of Xiangjiang and Jinjiang River in Changsha, China. It was air-dried, ground in a machine, and then sifted out. Only particles with a diameter less than 5 mm were reserved to provide a good combination with cement particles, resulting in uniform granularity of cemented soil. The detailed particle-size distribution of soil is presented in Fig. 1. The ordinary Portland cement with a strength grade of 42.5 MPa and GFRP tendons with 230 mm in height were selected to form GTRCS as pullout specimens. The alkali-free glass fiber (alkali content less than 0.8%) was used to produce GFRP tendon and the fiber volume fraction was 60%. The properties of GFRP tendon were tested by the Test Center of China Coal Research Institute. Table 1 presents the properties of the soil sample, cement, and GFRP tendons [49].

2.2. Mixture design

C_w, C_c, and T_c are the three main influence variables of GTRCS performance as mentioned before. Water and cement contents are defined as below:

$$C_w = \frac{m_w}{m_s} \quad (1)$$

$$C_c = \frac{m_c}{m_w + m_s} \quad (2)$$

where m_w means the weight of the water added; m_s is the weight of the dry soil; m_c denotes the weight of the cement.

C_w ranged from 50% to 90% in this study because areas where cemented stabilization is widely applied usually feature clay with water content near the liquid limit. C_c was designed between 6% and 30% to offer sufficient workability and optimum stabilization efficiency [5]. Besides, composites cured for 15–30 days are widely used in practice to solve problems such as tight schedules [51,52]. Hence, 5 stepwise increasing levels were chosen for C_w and C_c, and 6 levels for T_c with specific details shown in Table 2. In total, 150 GTRCS specimens were prepared in this study (5 levels for C_c × 5 levels for C_w × 6 levels for T_c).

2.3. Sample preparation

Generally, 'it is challenging to obtain the interface shear response of a full-length soil nail (normally several meters) because the nail is overlength. Meanwhile, sensors must be installed in an appropriate and representative location which is hard to achieve. Therefore, an element nail pullout cell (Fig. 2) was specially designed to address the difficulty involved in capturing key aspects of the various coupled relationships that affect soil-nail interaction [50]. The effective bond length of the tendon is set as 80 mm (around 1/100 of the actual length), representing a small fraction of the full-length nail in practice. This apparatus was supposed to determine the interface shear stress and relative displacement because of the negligible axial deformation of the tendon and constrained deformation of the soil [53]. The tendons in pullout cells had located the center before finishing the procedure of cemented soil transferring.

The raw materials to produce different proportional cemented soil mixtures were water, cement, and soil in this study, which were calculated from designing proportions (C_c, C_w). Dry soil and cement were mixed for 60 s to keep uniform before the water addition. The required amount of water was stirred with the dry mixture lasting 480 s, and conclusive wet cemented soil was then transferred into the cells for further curing. Prior to mixtures pouring, the base of the cell was decorated by the paper plate sealants to prevent concrete loss. The internal surface of the cell was wiped through lubricants to minimise the boundary friction, reducing the negative influence on the bonding strength measurement. Afterward, the cemented soil mixtures were vibrated and densified. Finally, the cells were cured in

Table 2 – Influence variables with all levels used in the experimental project [50].

Influence factor	Number of levels	Magnitude
Water content C_w (%)	5	50, 60, 70, 80, 90
Cement content C_c (%)	5	6, 12, 18, 24, 30
Curing duration T_c (days)	6	7, 14, 28, 42, 60, 90

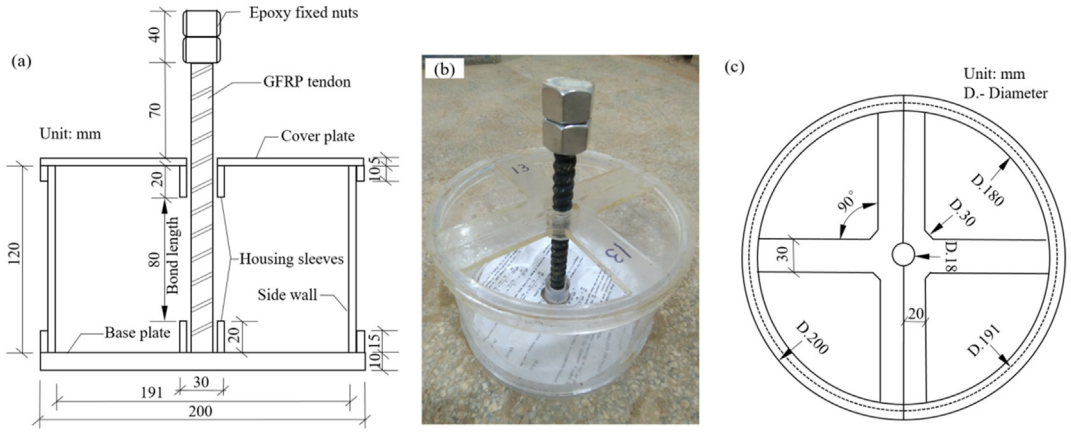

Fig. 2 – Diagrams of pullout cells with tendon (a) schematic diagram (b) side view (c) plan view [50].

plastic bags according to the predetermined design period. Plates of pullout cells should be removed after seven days, while compressive cells remain attached until curing is completed.

2.4. *Pullout test*

The pullout test apparatus used in this study is shown in Fig. 3, called pile interface friction testing system (PIFTS). To determine the interface bonding strength of GTRCS, pullout specimens were initially mounted to the traveling platform. Afterward, the tendon head was attached to the load cell through the connection cylinder. Specifically, two stacked epoxy nuts were fixed at the end of the tendon to enlarge the tendon head, as shown in Fig. 4a. The connection cylinder was presented in Fig. 4b, which was utilised to connect the load cell and the GFRP tendon. It consisted of upper and lower screw rings and a cylinder which was split into two parts to lock the enlarged tendon head. A threaded rod with a nut was used to connect the load cell to the upper screw ring through the central hole which was on the upper screw ring. The connection apparatus was carefully checked to ensure the capacity for the maximum pullout load.

The compatibility between pullout samples and equipment was controlled by tightening constraining plates as well as the platform. To minimise the misalignment of the tendon and load direction, the housing sleeves (20 mm) were set up in the cover and base plates, and a spherical joint was used at the top of the load cell, as shown in Figs. 2 and 3, respectively. Afterward, operators lowered the traveling platform at a 1.0 mm/min rate to transfer the load to GFRP tendons. This process terminated when platform displacement reached 20 mm, where tendons almost detached from their surrounding cemented soil matrix [16,54]. The interface shear stress was timely recorded by the top load cell. The relative displacement between the GFRP tendon and cemented soil (the pullout displacement of the tendon) was timely recorded by the bottom Linear Variable Differential Transformer (LVDT). In conclusion, the dataset of specimens' strength including T_p and T_t was summarized in the Appendix.

2.5. *Unconfined compression test*

Those compressive samples in cubic cells (10 cm side length) were utilised to determine compressive performances in this study. For equipment selection, the TYA-2000S Electron-Hydraulic compression machine was suitable because of its 0.01 KN accuracy. During the compression process, operators imposed a load rate at 0.03–0.15 kN/s until samples deformed sharply to be destroyed, determining the compressive capacities.

3. Multi-objective optimisation approach

The schematic illustrations of the whole process for MOFA-RF operation to obtain optimal GTRCS mixtures are shown in Fig. 5. The first step consisted of three RF model suggestions for predicting UCS, T_p, and T_t. During this process, two hyperparameters of RF were automatically adjusted by FA algorithm and 10-fold cross-validations (CV), which are the total number of regression trees (*numTree*) and the minimum sample number of a leaf node (*minNumLeaf*). In the meantime, the cost of each mixture was determined through defining the cost and density of each raw material, such as cement, water, and soil. The FA was then developed to MOFA for tri-objective design of GTRCS and a weighted sum approach was used for these three objectives. Ultimately, the Pareto front was subsequently constructed to demonstrate the GTRCS improvement blend plan. The ML and optimisation experiments were both implemented through Matlab R2020a.

3.1. *Data description*

As mentioned above, the variables are the cement proportion, water content, and curing period. These variables can be used to compute the mass ratio of the raw materials (cement, water, and soil). The outputs are the compressive strength and peak and residual pullout strengths with their datasets derived from the mechanical tests. Table 3 summarizes the basic database information for including raw materials and UCS, T_p, and T_t.

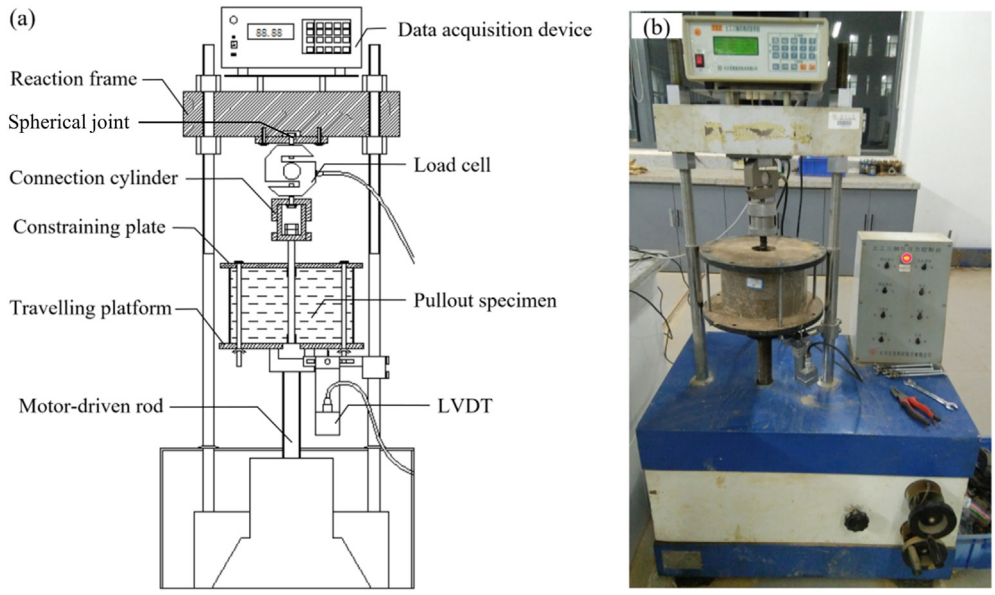

Fig. 3 – Diagram for pullout test apparatus [50].

Figure 6 shows the correlations between input variables based on the UCS, T_p, and T_t datasets. Only one correlation matrix was presented since the experimental mixture designs for UCS, T_p, and T_t are consistent. The relationships between input variables are visualized using a correlation matrix, representing the Pearson correlation coefficients between any two different variables. Pearson correlation coefficient is a commonly used method to evaluate the degree of correlation between variable X and variable Y. Most of the correlations between various components are less than 0.5, indicating that the input variables are unlikely to cause multicollinearity problems. The coefficient between cement and water is around 0.5 and others are close to zero. This is reasonability since they are designed based on the Cc (6%–30%) and Cw (50%–90%), while other variables are independent such as curing time, water content, and soil. The RF-FA model of the multi-object scheme was then proposed in this way.

3.2. *Establishment of FA-RF model*

3.2.1. *Random forest (RF)*

Random Forest creates hundreds of decision trees (RTs) to implement the final decision. RF model applies a 'bagging' way to integrate all the results derived from these RTs and utilises voting to acquire the peak results [55]. The bagging algorithm is proposed by Breiman [56], which effectively reduces the prediction variance and improves prediction performance. The RF algorithm is described in Fig. 7. Equation (3) shows the training set as R_n, where X and Y are the input vectors with m features ($X = \{x_1, x_2, \ldots, x_m\}$) and the output scalar, respectively.

During the training process for each RT, *n* samples from the training set are randomly sampled without replacement (1/n possibility for each sample to be selected at each time). This sample collecting process is called 'bootstrap' and the bootstrap sample set is symbolled as R_n^{θ}. Subsequently, the input

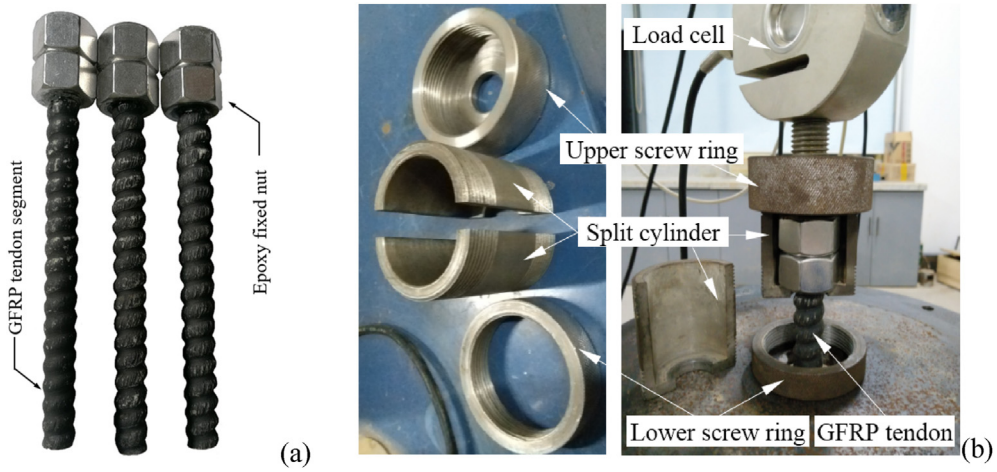

Fig. 4 – The images of (a) GFRP tendon and (b) connection cylinder [50].

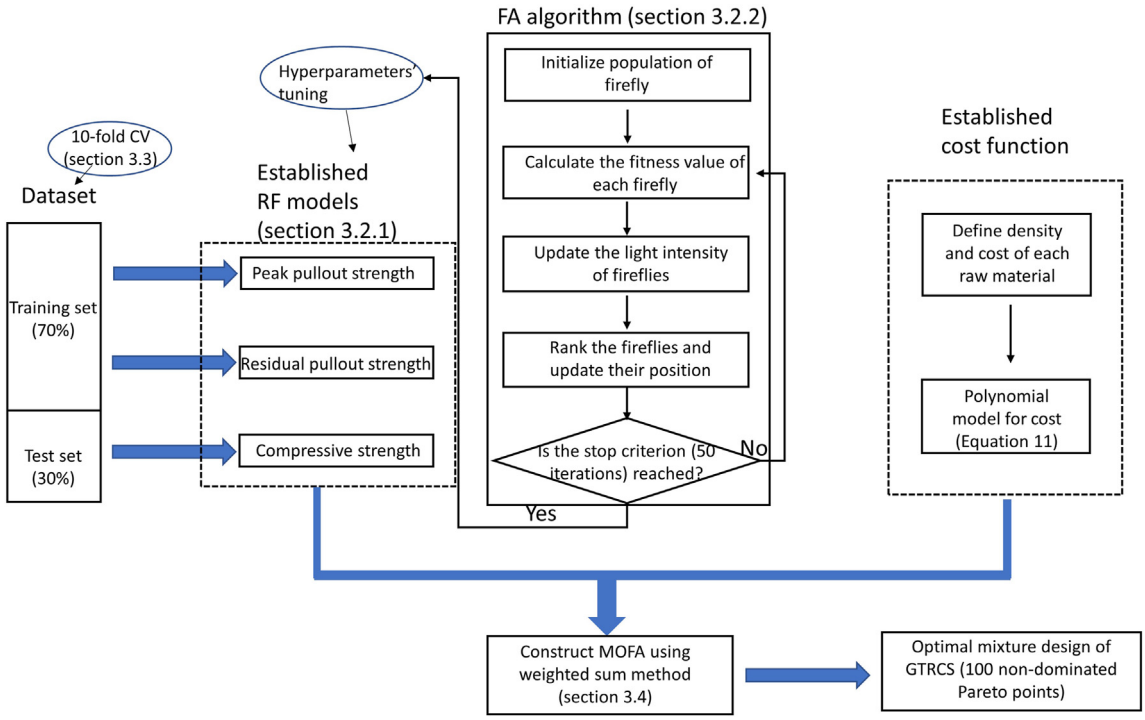

Fig. 5 – Schematic descriptions of the MOFA-RF system to obtain optimal GTRCS.

data R_n^{θ} are split from the root node to the leaf node by the algorithm. The prediction function $\hat{a}$ (X, R_n^{θ}) is constructed upon completing the RT training process. The random forest comprises k de-correlated RTs. Therefore, k prediction functions $\hat{a}$ (X, $R_n^{\theta_k}$), where $k = 1, 2, \ldots, k$, will be established. The symbol θ_k represents independently distributed random vector to distinguish these RTs. Finally, the RF produces k outputs $\{\widehat{Y}_1, \widehat{Y}_2, \ldots, \widehat{Y}_k\}$ corresponding to each RT. By averaging these outputs, as stated in Equation (4), the final prediction Y is obtained.

$$R_n = \{(X_1, Y_1), (X_2, Y_2), \ldots, (X_n, Y_n)\} \tag{3}$$

$$Y = \frac{1}{k}\sum_{i=1}^{k} \widehat{a}\left(X, R_n^{\theta_i}\right) \tag{4}$$

3.2.2. *Firefly algorithm (FA)*

The firefly algorithm is derived from the social behavior of fireflies [57]. Fireflies are attracted to the brightness so that the brighter firefly, the more attractive it is to others. However, the attractiveness of brightness decreases as the distance between two fireflies increases. The brightest firefly travels about the surroundings in a random pattern. Even though the other fireflies are constantly moving towards it, it will eventually be seen. Its objective function determines the brightness of an issue. Equation (5) depicts the position shift of firefly i as it moves closer to firefly j, which is brighter.

$$\mathbf{x}_i^{t+1} = \mathbf{x}_i^t + \beta_0 e^{-\gamma r_{ij}^2}\left(\mathbf{x}_j^t - \mathbf{x}_i^t\right) + \alpha(rand - 1/2) \tag{5}$$

$$r_{ij} = \left\|\mathbf{x}_j^t - \mathbf{x}_i^t\right\| \tag{6}$$

In the above function, $\mathbf{x}_i^t$ and $\mathbf{x}_j^t$ are the positions of two fireflies i and j at the t-th iteration. Besides, r_{ij} in Equation (6) shows the Euclidian distance between the positions of the two fireflies and β_0 means the highest attractiveness of the firefly when r equals zero. Considering the brightness of distance and medium reduces, γ is introduced as an absorption coefficient (0–1). Besides, α and *rand* are the randomization parameter and random vector derived from the Gaussian

Table 3 – Input and output variables in the UCS, T_p, and T_t aspect.

Variables	Minimum	Maximum	Medium	Mean	Std Dev	CV
Cement (kg/m^3)	86.67	438.02	259.46	256.33	113.35	0.44
Water (kg/m^3)	486.69	684.22	593.54	588.72	51.92	0.09
Soil (kg/m^3)	681.50	1102.10	847.92	863.48	117.52	0.14
Curing age (day)	7	90	35	40	28	0.7
UCS (kPa)	31.18	10255.10	1274.15	2215.78	2213.69	1.05
T_p (kPa)	3	5363.07	419.25	954.13	1169.73	1.23
T_t (kPa)	0.29	1109.60	74.56	179.52	224.56	1.25

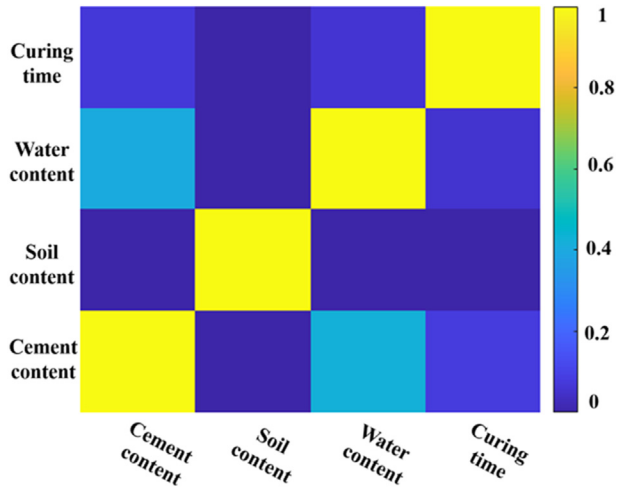

Fig. 6 – Correlation diagram of influencing factors in mechanical performance.

distribution, ranging from 0 to 1. The pseudocode of FA can be shown in Fig. 8.

3.3. Cross fold validation

The overfitting problem caused by the limited amount of data is a complex problem, which can be solved by 10-fold cross-validation (CV) shown in Fig. 9. Specifically, the dataset was first randomly divided into two parts: test fold and training fold, which accounted for 30% and 70% of the whole dataset, respectively. Then, the training fold was further randomly segmented to ten sets where nine sets (internal training set) aimed at model training. The remaining one set (validation set) was used to calculate root-mean-square error (RMSE) values. In the process of model training, FA algorithm was implemented to update the hyperparameters within 50 iterations through seeking the minimum RMSE [58]. The model training and validation process was repeated ten times (i.e., 10-fold CV). Ultimately, 10 RF models were established and the one with the least RMSE value was chosen as the final model, to further evaluate its performance on the test set.

In this research, the root mean square error (RMSE), correlation coefficient (R), mean absolute percentage error (MAPE), and mean absolute error (MAE) employed to assess the ML models' characteristics are defined as:

$$RMSE = \sqrt{\frac{1}{N}\sum_{i=1}^{N}\left(y_i^* - y_i\right)^2} \tag{7}$$

$$R = \frac{\Sigma_{i-1}^{N}\left(y_i^* - \overline{y^*}\right)\left(y_i - \overline{y}\right)}{\sqrt{\Sigma_{i=1}^{N}\left(y_i^* - \overline{y^*}\right)^2}\sqrt{\Sigma_{i=1}^{N}\left(y_i - \overline{y}\right)^2}} \tag{8}$$

$$MAPE = \frac{1}{N}\sum_{i=1}^{n}\left|\frac{y_i^* - y_i}{y_i}\right| \tag{9}$$

$$MAE = \frac{1}{N}\sum_{i=1}^{n}\left|y_i^* - y_i\right| \tag{10}$$

where the number of samples in the dataset is denoted by N; the predicted output of ML models is denoted by y_i^*; the actual output in the dataset is denoted by y_i; the projected mean value is $\overline{y^*}$, whereas the actual mean value in the dataset is b $\overline{y}$.

3.4. Multi-objective optimisation

3.4.1. Objective function establishment

The representation function of UCS, T_p, and T_t are the known FA-RF models. Meanwhile, the following is how the polynomial function is utilised as the cost objective function:

$$Cost\left(\$ / m^3\right) = C_c Q_c + C_w Q_w + C_s Q_s \tag{11}$$

In Equation (11), Q_w, Q_s, Q_c represents the amount (kg/m^3) of water, soil, and cement, respectively. In the case of C, it denotes the unit pricing (kg/m3) of GTRCS components, as given in Table 4.

3.4.2. Constraints

The following restrictions must be set for MOO issues: material range, volume, and ratio limitations. The data scope is derived from GTRCS files that determine the raw material top and bottom limits. The volume restrictions show that the quantity of cemented soil should be kept to a maximum of one cubic meter shown in Equation (12):

$$V_m = \frac{Q_c}{U_c} + \frac{Q_w}{U_w} + \frac{Q_s}{U_s} \tag{12}$$

where U_c, U_w, and U_s are unit weights of cement, water, and soil, respectively.

Furthermore, fixed ratios are regulated for the correlation establishment of different raw materials to find the best GTRCS composition. These limitations are summarized in Table 5.

3.4.3. MOFA-RF establishment

The MOFA-RF is created by merging the UCS, T_p, and cost objective functions. There are many useful methods to solve multi-objective optimisation problems, including the weighted sum approach, ε-constraint, global criterion method, goal programming, and the complex method [59]. Among these approaches, the weighted sum method is one of the most widely used approaches mainly due to its simplicity. The weighted sum method changes weights systemically, and each different single objective optimisation determines a different optimal solution. These solutions obtained approximate the Pareto front. This method has been used to develop many multi-objective optimisation algorithms, such as multi-objective cuckoo search [59] and multi-objective optimisation algorithm [60]. Therefore, the weighted sum is employed in this research and function F is shown as follows:

$$F = \sum_{k=1}^{k} w_k f_k\,,\ \sum_{k=1}^{k} w_k = 1 \tag{13}$$

where f_k is the objective function; weights (w_k) are calculated as $\frac{p_k}{K}$; p_k is the random value (from 0 to 1) with uniform distribution. In this study, two tri-objective functions showing

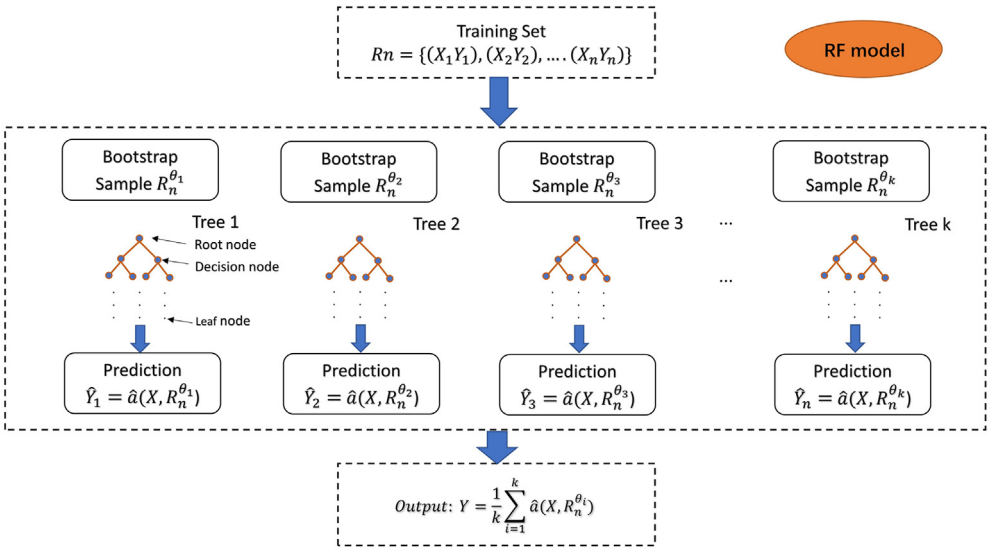

Fig. 7 – Construction of an RF model.

the relationship between UCS, cost, and T_p can be defined as follows:

$$F_1 = w_1 \cdot UCS\ (90\ days) + w_2 \cdot T_p\ (90\ days) + w_3 \cdot cost\ \ F_2 = w_1 \cdot UCS\ (90\ days) + w_2 \cdot T_t\ (90\ days) + w_3 \cdot cost \quad (14)$$

$$\sum_{k=1}^{3} w_k = 1 \quad (15)$$

The Pareto front is advised for optimising multi-purpose objectives by providing non-dominate solutions [61]. Other objectives cannot be improved without degradation as a result of this situation. If Z is the group of feasible solutions and $\mathbf{x}^* \in Z$ is one of the Pareto points, $\mathbf{x}^*$ can be recognised that no existence of $\mathbf{x} \in Z$ could satisfy:

$$f_k(\mathbf{x}) \le f_k(\mathbf{x}^*)\ for\ k = 1, 2, 3, \ldots, t\ and \quad (16)$$

$$f_k(\mathbf{x}) < f_k(\mathbf{x}^*)\ for\ atleast\ one\ k \quad (17)$$

If $f(\mathbf{x}^*)$ is larger than $f(\mathbf{x})$ for every $\mathbf{x}$, Pareto optimal solution $\mathbf{x}^*$ will be achieved. The Pareto front, seen in Fig. 10, is made up of multiple Pareto points. The MOFA is proposed in this work based on the FA algorithm using the

Begin
Define objective function $f(x)$, $x = (x_1, \ldots, x_d)^T$
Set the search space, total number of generations, and fireflies
Obtain light intensity I_i at x_i by $f(x_i)$
Set light absorption coefficient
Generate initial population, $k = 0$
While $(t \le maxGeneration)$
    Update the generation number, $k = k + 1$
    Tune randomisation parameter using adaptive inertia weight
    Tune attractiveness parameter using Guass/mouse chaotic map
        for $i = 1$: no. fireflies
            for $j = 1$: no. fireflies
                if $(I_j > I_i)$
                    move firefly i toward j by levy flight
                end if
                change attractiveness with distance r
            end for j
        end for i
        Rank the fireflies and find the current best
end while
Obtain results
End

Fig. 8 – The pseudocode of FA.

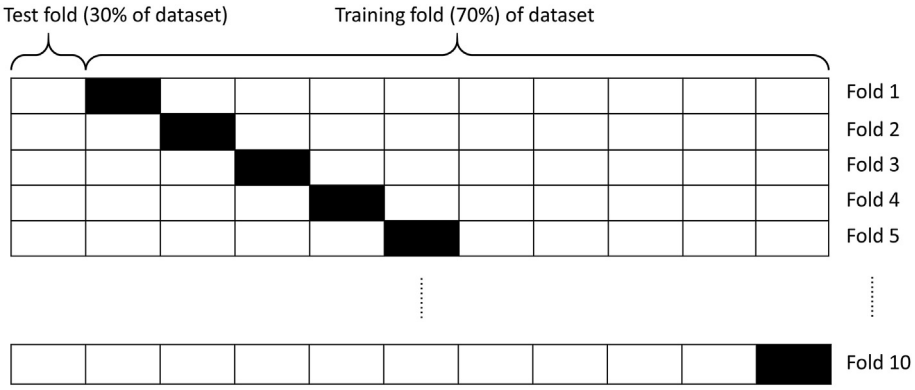

Fig. 9 – 10-Fold cross-validation.

weight sum technique, with the pseudocode summarized in Fig. 11.

3.4.4. *Decision-making for MOO*

As previously demonstrated, the Pareto front may be utilised to solve MOO issues, but the peak optimal mixing percentage is insufficient for decision-making. As a result, in this work, the Technique for Order Preference by Similarity to Ideal Solution (TOPSIS) is presented [62]. It can pick a solution that is closest to the positive ideal point (d_{i+}) and farthest from the negative ideal point (d_{i-}) simultaneously. The d_{i+} and d_{i-} are the objective function's best value and worst value, respectively. As a result, using the formulae below, the solution with the highest C_i is considered the best:

$$d_{i+} = \sqrt{\sum_{j=1}^{n} \left(F_{ij} - F_j^{ideal}\right)^2} \tag{18}$$

$$d_{i-} = \sqrt{\sum_{j=1}^{n} \left(F_{ij} - F_j^{non-ideal}\right)^2} \tag{19}$$

$$C_i = \frac{d_{i-}}{d_{i+} + d_{i-}} \tag{20}$$

where n is the total objective number and i represents the ith Pareto point; F_j^{ideal} and $F_j^{non-ideal}$ are the ideal and non-ideal values of the jth objective, respectively.

3.5. *Variable importance measure*

The relationship between inputs variables and output was evaluated using global sensitivity analysis (GSA). When the input value varies within its value range, it can measure the change of the established RF-FA output results [63]. Each variable is examined independently when the other variables maintain their mean values. The equations below offer a gradient metric for evaluating output change and the relative significance formulation. Specifically, the data sample is represented as x, and x_a, $a \in \{1, \ldots, M\}$ denotes an input variable through its range with L levels (M is the number of input variables). The symbol y represents the output value which is predicted by the RF-FA. According to the value range of x_a and L levels, the input variable x_a can be divided into i values, namely, x_{ai}, $i = \{1, \ldots, L\}$. The symbol $\widehat{y_{a,i}}$, $i = \{1, \ldots, L\}$ stands for the sensitivity response indicator for x_{ai}, $i = \{1, \ldots, L\}$.

$$g_a = \sum_{i=2}^{L} \frac{|\widehat{y_{a,i}} - \widehat{y_{a,i-1}}|}{L-1} \tag{21}$$

$$R_a = g_a \Big/ \sum_{i=1}^{L} g_i \tag{22}$$

Table 4 – The unit cost of each variable of GTRCS.

Variables	Notation	Unit price ($/kg)	Unit weight (kg/m^3)
OPC	C_c	0.057	3100
Water	C_w	0.001	1000
Soil	C_s	0.014	2650

Table 5 – The constraints of GTRCS input variables.

Variables	Expressions	Lower limit	Upper limit
OPC	C_c	87	438
Water	C_w	487	684
Soil	C_s	681	1102
Water content	C_w/C_s	0.5	0.9
Cement content	$C_c/(C_w + C_s)$	0.06	0.3

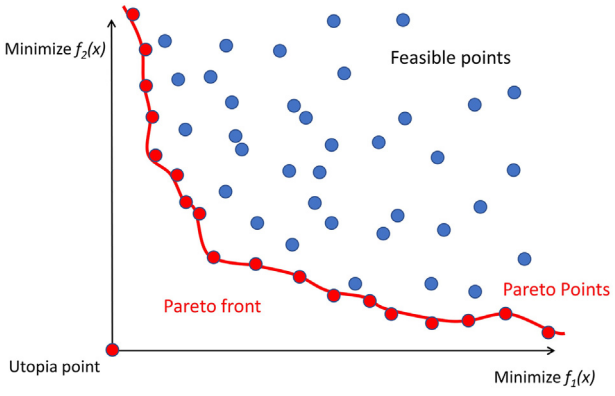

Fig. 10 – Pareto front and feasible points.

Begin
Define objective function $f_1(x),\ f_2(x), \ldots, f_k(x); x = (x_1, \ldots, x_d)^T$
Generate initial population of fireflies $x_i = (i = 1,2, \ldots, n)$
Determine light intensity I_i at x_i by $f(x_1)$
Set light absorption coefficient
While
    for $i, j = 1{:}n$ (all n fireflies)
        Evaluate the approximations of PF_i and PF_j to the Pareto front
            if PF_j dominates PF_i,
                Move firefly from i to j
                Generate new ones if constraints are not satisfied
            end if
            if no non-dominated solutions can be found
                Generate random weights $w_k(k = 1, \ldots K)$
                Find the best solution that can minimise the combined objective
                Random walk around the best solution
            end if
            Update and pass the non-dominated solutions to the next iterations
    end
    Sort and find the current best approximation to the Pareto front
    Update t
end while
Post process results and visualisation

Fig. 11 – The pseudocode of MOFA.

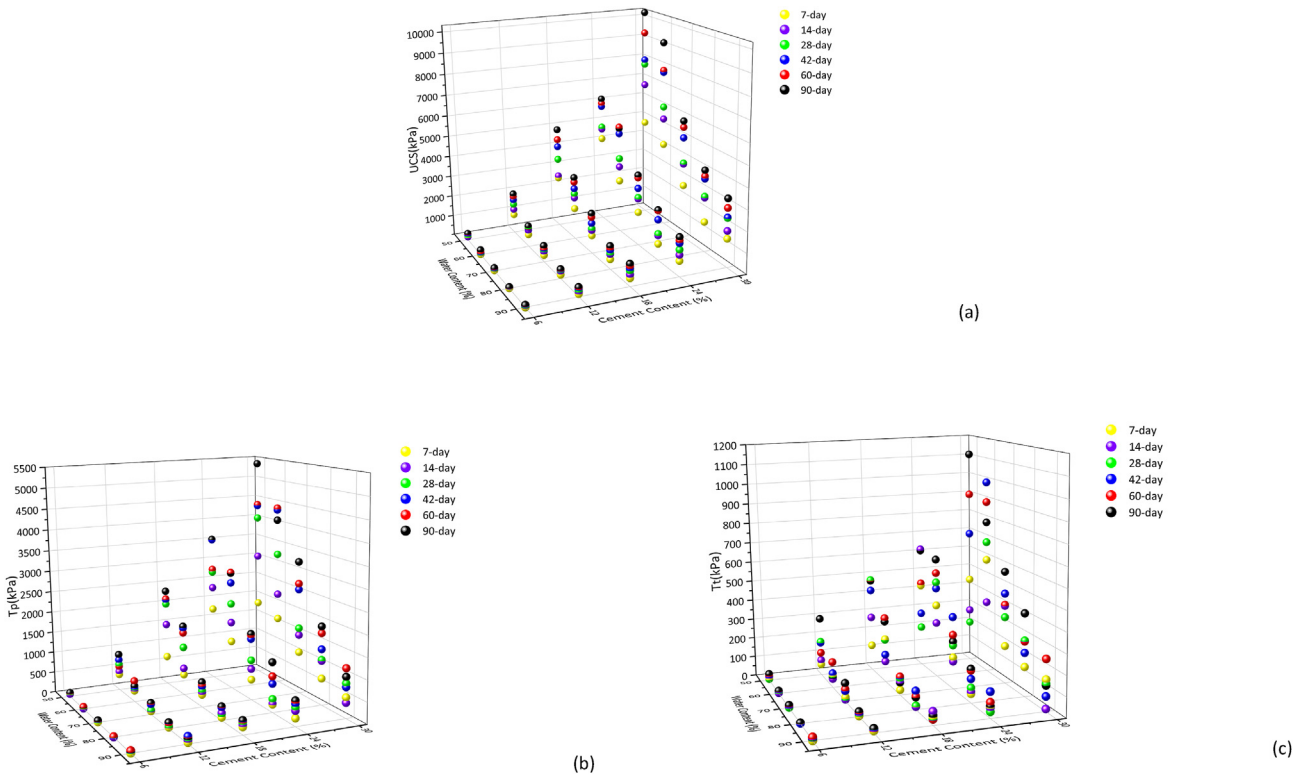

Fig. 12 – Strength diagrams for soil mixtures including different water and cement content under varying curing periods (a) UCS (b) T_p (c) T_t.

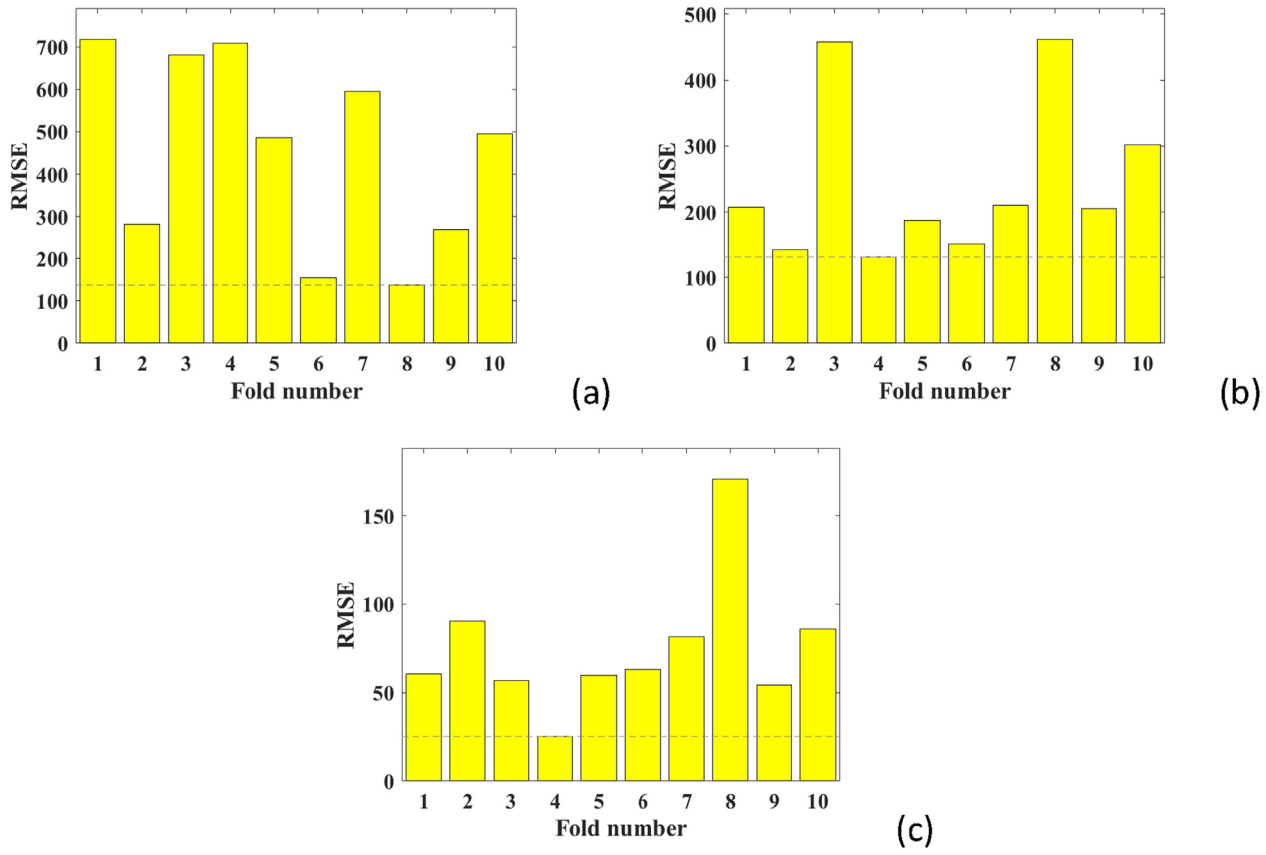

Fig. 13 – RMSE of 10-fold CV for on the (a) UCS (b) T_p (c) T_t dataset.

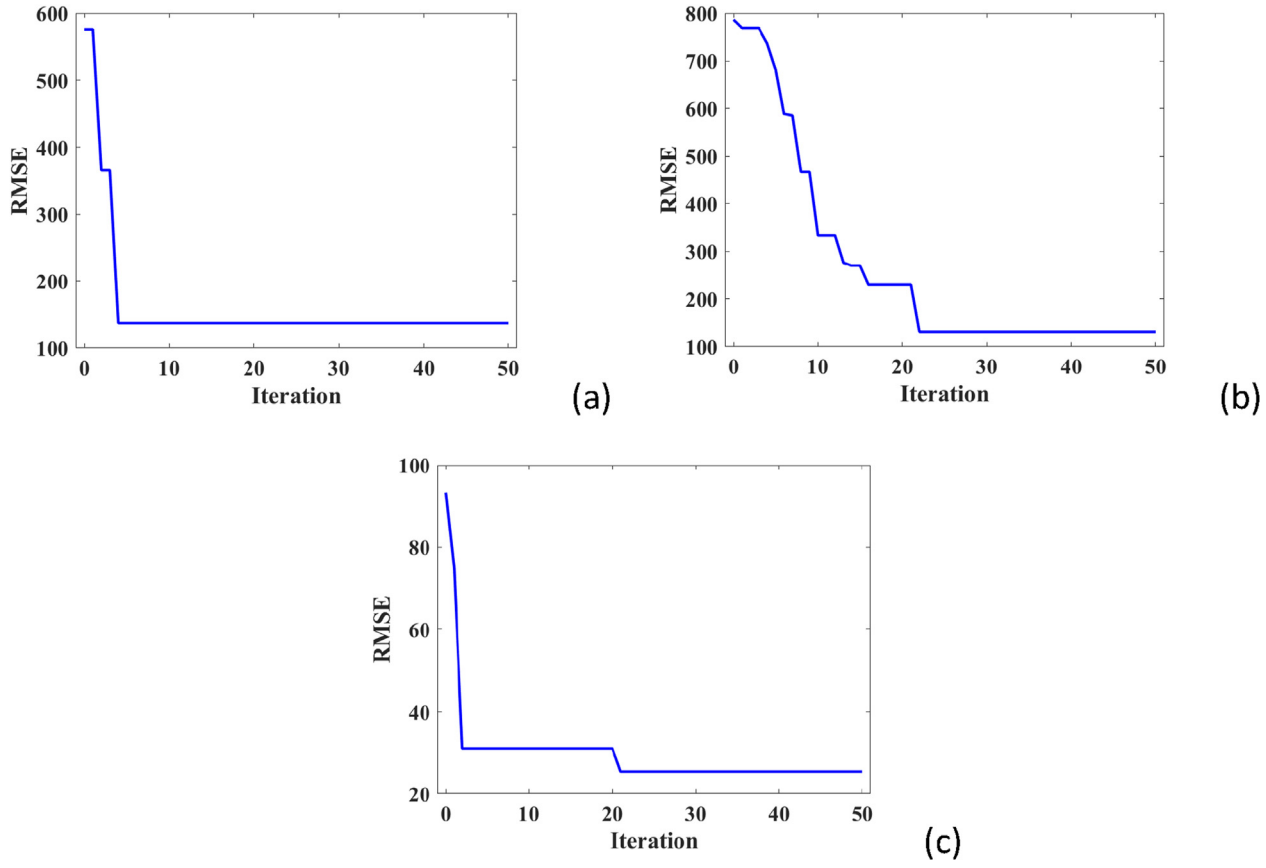

Fig. 14 – RMSE iteration in the optimal fold of (a) UCS (b) T_p (c) T_t dataset.

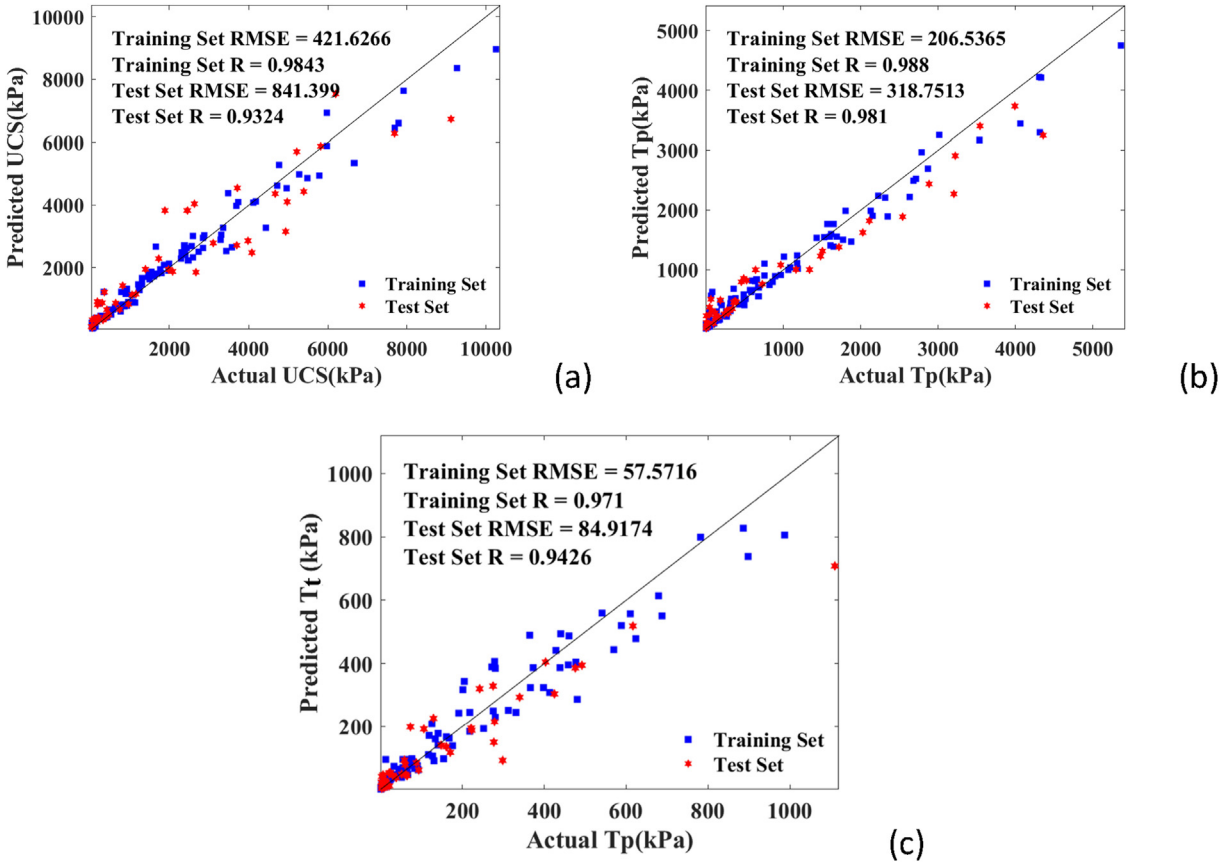

Fig. 15 – Actual versus predicted values for (a) UCS (b) T_p (c) T_t.

where g_a is a gradient metric and R_a is the relative importance of the variable x_a.

4. Results and discussion

4.1. *Results of laboratory tests*

Figure 12 depicts relationships between varying input variables (C_c, C_w and T_c) and experimental mechanical performances, including UCS, T_p, and T_t of GTRCS. The curing time exerted a negligible effect on the UCS and T_p of specimens owning 6% cement content, which was attributed to the completed hydration reaction at the early stage with inadequate cement addition. Nevertheless, the compressive strength and pullout strength of GTRCS both rose sharply with curing time extension when cement content increased to 30%. The possible explanation was that cement increment led to greater amounts of stabilising hydration products. Meanwhile, longer curing time results in more thorough hydration reaction and more hydration components, behaving gathered dense behaviour instead of separated components. Unlike the positive consequences of C_c and T_c, C_w imposed negative impacts on the GTRCS performances, which weakened the microstructure of the whole mixture by rising porosity. Regarding the residual pullout strength, the general increasing trend was observed when increasing cement content. It was also positively related to the curing time although some fluctuations occurred which might be caused by the experimental error. A detailed progressive failure of tendon-cemented soil interface was reported by Chen et al. (2021) [50]. In conclusion, the mechanical strengths of GTRCS (UCS, T_p, T_t) were positively controlled by influencing factors (C_c, T_c), converse to C_w.

4.2. *Modelling results*

4.2.1. *Results of hyperparameter tuning*

As previously indicated, the two hyperparameters of the RF model (*numTree*, *minNumLeaf*) were tuned using FA and 10-fold CV. The ideal fold within 10 folds CV provides the lowest RMSE, which is shown in Fig. 13. On the UCS, T_p, and T_t

Table 6 – Evaluation index of UCS, T_p and T_t modelling in the training set.

Test category	Evaluation index			
	RMSE (kPa)	R	MAE (kPa)	MAPE
UCS	841.40	0.932	591.64	0.765
T_p	318.75	0.981	219.92	1.322
T_t	84.92	0.943	49.53	1.103

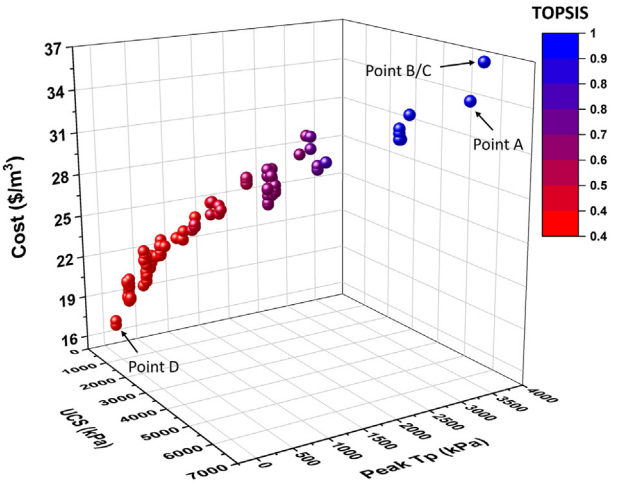

Fig. 16 – Pareto fronts of UCS, cost, and T_p for GTRCS (90 days).

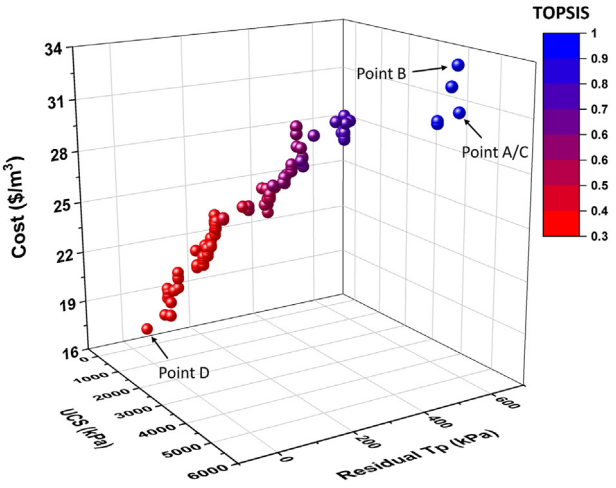

Fig. 17 – Pareto fronts of UCS, cost, and T_t for GTRCS (90 days).

datasets, the minimum RMSE was found at the 8th, 4th, and 4th folds, respectively. The corresponding RMSE iteration processes in these folds are illustrated in Fig. 14. It was observed that 5, 23, and 22 iterations were required to obtain the minimum RMSE values, demonstrating the feasibility and efficiency of adjusting the hyperparameters via the FA algorithm. Finally, the hyperparameters of established RF models were: UCS (*numTree* = 7, *minNumLeaf* = 1), T_p (*numTree* = 14, *minNumLeaf* = 1), T_t (*numTree* = 14, *minNumLeaf* = 1).

4.2.2. *Performance of FA-RF*

The predicting performance of existing FA-RF models on both training and test sets is intuitively depicted in Fig. 15. The closer distance between the points and the black solid diagonal line indicates the smaller error between actual and predicted values. Most points were close to the diagonal line showing that the three established FA-RF models generally provided accurate predictions on all of the datasets. Table 6 summarises the values of the FA-RF models' four evaluation indicators (R, RMSE, MAE, and MAPE) for the prediction of UCS and T_p and T_t on the test set. The R values were 0.9324, 0.981, and 0.9426, respectively, indicating the low error between the anticipated and actual results. Meanwhile, relatively low RMSE, MAE, and MAPE values also verified the model prediction accuracy. Besides, the RMSE or R values on the training and test sets were similar so that the risk of overfitting or underfitting problem was low.

4.2.3. *GTRCS mixture optimisation*

After establishing three FA-RF models, the MOFA-RF was proposed to minimise the objective function using the weighted sum method. The objective of this study was to maximise the 90-day UCS and pullout strength and simultaneously minimise the cost. Finally, the Pareto front of the tri-objective (UCS, cost, and T_p) optimisation design was achieved shown in Fig. 16. In total, 100 non-dominated Pareto points were generated in the Pareto front and they presented an appropriate UCS, cost, and T_p relationship, suggesting the effectiveness of MOFA-RF model. To improve GTRCS mechanical performance (i.e., UCS and T_p), the cost must be increased. This is reasonable since larger cement content results in higher mechanical strength and cement cost is relatively higher than both water and soil.

Among the 100 non-dominated points, points A, B, C, and D are four particular points corresponding to the single goal optimisation design (highest TOPSIS, maximum UCS, maximum T_p, and lowest cost). In Fig. 16, the 90-day UCS and T_p simultaneously reached the peak values at 6139.51 kPa and 3632.70 kPa, respectively (point B/C). Besides, the least cost (17.01 \$/m^3) was discovered at point D, whereas the UCS and T_p were significantly diminished. Point A was judged to be the optimal solution according to the TOPSIS theory, providing an appropriate relationship between the three objectives. This

Table 8 – Mixture proportions of Pareto solutions of GTRCS (90 days).

Point	Cc	Cw	UCS (kPa)	T_p (kPa)	Cost (\$/m^3)	TPOSIS
A/C	22.43%	64.12%	5224.04	557.25	31.32	1
B	25.35%	60.76%	5268.02	545.94	33.89	0.96
D	6.99%	85.23%	384.34	20.43	17.49	0.30

Table 7 – Mixture proportions of Pareto solutions of GTRCS (90 days).

Point	Cc	Cw	UCS (kPa)	T_p (kPa)	Cost (\$/m^3)	TPOSIS
A	26.55%	63.21%	5983.04	3507.88	34.22	1
B/C	29.40%	59.41%	6139.51	3632.70	36.80	0.97
D	6.82%	88.71%	494.65	57.60	17.01	0.41

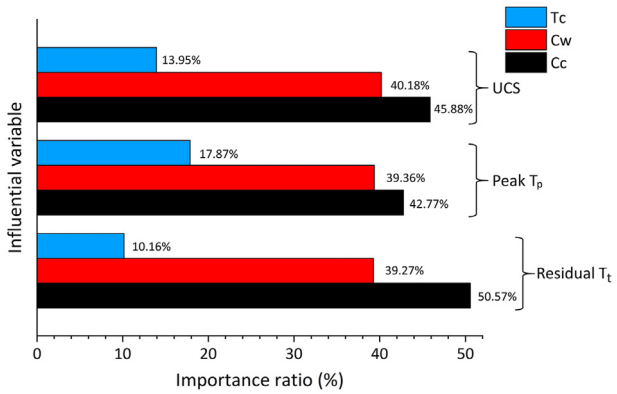

Fig. 18 – The relative importance of each variable on UCS, T_p, and T_t of GTRCS mixture optimisation.

point achieved the highest TOPSIS score of 1with 5983.04 kPa UCS, 3507.88 kPa T_p, and a cost of 34.22 \$/m^3. Table 7 shows the corresponding mixing proportions of solutions A, B, C, and D.

Similarly, another Pareto front was successfully obtained when the T_p was replaced as T_t shown in Fig. 17. The single objective optimisation design corresponds to Point A, B, C, and D showing the maximum TOPSIS score, UCS, T_t, and minimum cost at 1, 5268.02 kPa, 557.25 kPa, and 17.49 \$/m^3, respectively. The cement ratio and water content of each design solution are presented in Table 8. In general, the TOPSIS method automatically provides a design recommendation for decision-makers. However, the final decision should be made under specific circumstances.

4.2.4. *Variable significance*

Figure 18 shows the significance percentage of each input variable for GTRCS. The cement content possessed the highest important ratio at 45.88%, 42.77%, and 50.57%, respectively, concerning UCS, T_p, and T_t. This finding agreed with the experimental analysis that cement ratio remarkably influenced the mechanical performance of GTRCS. Besides, the water ratio was the second important variable since it determined the water to cement ratio. The curing time was the least essential variable compared to water and cement ratios, reaching only 13.95%, 17.87%, and 10.16% for UCS, T_p, and T_t. This is mainly resulted from the less effect of curing time than cement/water ratio on strength at late stage (e.g., 90 days), which is indicated by the strength evolution curve.

5. Conclusions

This study conducted the compressive and pullout tests to investigate UCS and the interface bond strength (peak and residual) between the cemented soil and GFRP tendons. Based on the laboratory tests results, the Pareto fronts were successfully achieved through proposing MOFA-RF. The main conclusions were depicted as follows.

- The mechanical properties (UCS, T_p, and T_t) of GTRCS were positively related to cement content and curing age, whereas they were negatively related to water content. This phenomenon can be attributed to the thorough cement hydration and increased hydrated product when cement content is high, water content is low, and curing time is long.
- The FA-RF models were successfully established on all the datasets with high values of correlation coefficients (UCS: 0.9324, T_p: 0.981, T_t: 0.9426) and low RMSE values (UCS: 841.40 kPa, T_p: 318.75 kPa, T_t: 84.92 kPa). However, the proposed models have their specificity on the laboratory data. Thereby, model revision is required for field data considering the inevitable difference between the laboratory and field test results.
- The Pareto fronts for tri-objective optimisation based on MOFA-RF were successfully obtained, providing feasible design solutions for decision-makers. Apart from the specific requirements, the solution with the highest TOPSIS is preferable.
- From sensitivity analysis, the cement content was the most significant influencing factor, followed by water content and curing time.

Data availability statement

All data, models, and code generated or used during the study appear in the submitted article.

Declaration of Competing Interest

The authors declare that they have no known competing financial interests or personal relationships that could have appeared to influence the work reported in this paper.

Acknowledgements

This work was sponsored by the National Natural Science Foundation of China (grant numbers 51908201 and 51978254), Natural Science Foundation of Hunan Province (grant number 2020JJ5024), and the Key R&D Project of Hunan Province Intelligent Disaster Prevention and Mitigation and Ecological Restoration in Civil Engineering (grant number 2020SK2109). Meanwhile, this work was supported by Hunan Key Laboratory of Intelligent Disaster Prevention and Mitigation and Ecological Restoration in Civil Engineering, Hunan Provincial Engineering Research Center, Catastrophe and Reinforcement of Dangerous Engineering Structures. This research is also funded by Academic Research Council of Australia Linkage Projects for Asset Intelligence: Maximising Operational Effectiveness for Digital Era, (Grant No. LP180100222).

Appendix

Specimen	Cc	Cw	Tc (day)	UCS (kPa)	Tp (kPa)	Tt (kPa)	Specimen	Cc	Cw	Tc (day)	UCS (kPa)	Tp (kPa)	Tt (kPa)
C06W50T07	0.06	0.50	7	186.43	53.77	6.18	C24W50T07	0.24	0.50	7	4176.33	1768.69	427.87
C06W50T14	0.06	0.50	14	182.38	53.23	18.55	C24W50T14	0.24	0.50	14	4666.67	2317.43	623.72
C06W50T28	0.06	0.50	28	219.86	70.58	5.72	C24W50T28	0.24	0.50	28	4770.39	2713.37	201.71
C06W50T42	0.06	0.50	42	304.08	72.47	19.89	C24W50T42	0.24	0.50	42	5817.69	3532.53	278.01
C06W50T60	0.06	0.50	60	337.41	79.31	24.64	C24W50T60	0.24	0.50	60	5979.59	2785.21	440.90
C06W50T90	0.06	0.50	90	358.50	92.08	33.25	C24W50T90	0.24	0.50	90	6197.96	3541.76	616.45
C06W60T07	0.06	0.60	7	43.51	15.75	3.32	C24W60T07	0.24	0.60	7	2585.33	1174.05	372.67
C06W60T14	0.06	0.60	14	54.54	7.39	2.56	C24W60T14	0.24	0.60	14	3297.28	1646.52	280.09
C06W60T28	0.06	0.60	28	68.76	13.54	4.70	C24W60T28	0.24	0.60	28	3708.16	2110.42	491.98
C06W60T42	0.06	0.60	42	108.82	49.09	10.33	C24W60T42	0.24	0.60	42	4948.98	2628.90	460.41
C06W60T60	0.06	0.60	60	150.14	49.88	12.61	C24W60T60	0.24	0.60	60	5272.79	2883.32	540.31
C06W60T90	0.06	0.60	90	268.37	46.06	13.90	C24W60T90	0.24	0.60	90	5212.24	2868.55	610.27
C06W70T07	0.06	0.70	7	54.29	7.02	2.34	C24W70T07	0.24	0.70	7	1654.22	494.43	160.91
C06W70T14	0.06	0.70	14	70.80	9.95	2.49	C24W70T14	0.24	0.70	14	2319.09	753.74	140.10
C06W70T28	0.06	0.70	28	83.40	9.95	2.05	C24W70T28	0.24	0.70	28	2383.27	965.03	222.70
C06W70T42	0.06	0.70	42	130.82	30.95	7.46	C24W70T42	0.24	0.70	42	2837.41	1480.38	365.71
C06W70T60	0.06	0.70	60	140.35	34.44	10.99	C24W70T60	0.24	0.70	60	3353.06	1571.07	275.01
C06W70T90	0.06	0.70	90	169.46	46.63	13.68	C24W70T90	0.24	0.70	90	3478.23	1605.97	242.19
C06W80T07	0.06	0.80	7	41.88	10.53	3.22	C24W80T07	0.24	0.80	7	822.31	192.02	45.56
C06W80T14	0.06	0.80	14	52.65	3.00	1.36	C24W80T14	0.24	0.80	14	1228.30	213.72	55.99
C06W80T28	0.06	0.80	28	58.45	4.61	1.15	C24W80T28	0.24	0.80	28	1309.97	323.51	75.90
C06W80T42	0.06	0.80	42	61.46	12.39	0.98	C24W80T42	0.24	0.80	42	1983.67	683.24	119.07
C06W80T60	0.06	0.80	60	73.91	16.10	3.47	C24W80T60	0.24	0.80	60	2425.65	857.21	160.91
C06W80T90	0.06	0.80	90	86.26	13.36	3.56	C24W80T90	0.24	0.80	90	2448.98	1187.54	168.34
C06W90T07	0.06	0.90	7	31.18	3.46	0.29	C24W90T07	0.24	0.90	7	781.36	192.74	53.48
C06W90T14	0.06	0.90	14	52.87	28.18	8.57	C24W90T14	0.24	0.90	14	1059.83	363.78	51.73
C06W90T28	0.06	0.90	28	62.24	27.52	4.97	C24W90T28	0.24	0.90	28	1305.10	439.46	32.37
C06W90T42	0.06	0.90	42	120.39	28.77	4.90	C24W90T42	0.24	0.90	42	1607.55	520.62	127.63
C06W90T60	0.06	0.90	60	122.31	57.09	15.86	C24W90T60	0.24	0.90	60	1734.35	577.49	77.37
C06W90T90	0.06	0.90	90	136.26	41.84	8.48	C24W90T90	0.24	0.90	90	1891.84	597.72	59.68
C12W50T07	0.12	0.50	7	933.88	386.33	54.84	C30W50T07	0.30	0.50	7	4715.90	1804.11	438.98
C12W50T14	0.12	0.50	14	1209.18	463.54	77.87	C30W50T14	0.30	0.50	14	6657.82	3014.98	271.80
C12W50T28	0.12	0.50	28	1468.98	647.42	175.64	C30W50T28	0.30	0.50	28	7695.24	3992.32	204.32
C12W50T42	0.12	0.50	42	1692.52	755.99	170.52	C30W50T42	0.30	0.50	42	7916.33	4303.62	687.53
C12W50T60	0.12	0.50	60	1868.03	589.84	116.95	C30W50T60	0.30	0.50	60	9260.82	4332.55	898.01
C12W50T90	0.12	0.50	90	2003.61	889.72	298.42	C30W50T90	0.30	0.50	90	10255.10	5363.07	1109.60
C12W60T07	0.12	0.60	7	623.95	265.83	60.55	C30W60T07	0.30	0.60	7	4104.90	1614.29	588.30
C12W60T14	0.12	0.60	14	835.46	277.12	44.27	C30W60T14	0.30	0.60	14	5389.29	2226.53	365.18
C12W60T28	0.12	0.60	28	967.62	314.72	58.58	C30W60T28	0.30	0.60	28	5980.95	3221.78	679.72
C12W60T42	0.12	0.60	42	933.33	328.26	73.22	C30W60T42	0.30	0.60	42	7687.07	4312.24	986.65
C12W60T60	0.12	0.60	60	934.00	505.89	130.73	C30W60T60	0.30	0.60	60	7782.31	4358.19	886.65
C12W60T90	0.12	0.60	90	1055.10	384.18	54.31	C30W60T90	0.30	0.60	90	9115.65	4063.76	782.51
C12W70T07	0.12	0.70	7	354.08	77.13	21.73	C30W70T07	0.30	0.70	7	2621.32	1010.63	190.99
C12W70T14	0.12	0.70	14	535.05	79.88	9.18	C30W70T14	0.30	0.70	14	3689.12	1432.39	397.89
C12W70T28	0.12	0.70	28	577.55	105.62	11.41	C30W70T28	0.30	0.70	28	3732.65	1599.84	339.86
C12W70T42	0.12	0.70	42	644.56	244.34	51.56	C30W70T42	0.30	0.70	42	4969.39	2541.44	459.53
C12W70T60	0.12	0.70	60	668.03	273.12	61.39	C30W70T60	0.30	0.70	60	5480.27	2680.36	403.2642
C12W70T90	0.12	0.70	90	816.46	277.08	91.11	C30W70T90	0.30	0.70	90	5780.27	3203.88	570.11
C12W80T07	0.12	0.80	7	209.93	29.70	2.88	C30W80T07	0.30	0.80	7	1481.50	640.16	148.2539
C12W80T14	0.12	0.80	14	376.05	40.58	11.14	C30W80T14	0.30	0.80	14	2660.45	1061.03	276.79
C12W80T28	0.12	0.80	28	384.45	48.03	7.11	C30W80T28	0.30	0.80	28	2720.88	1086.54	278.52
C12W80T42	0.12	0.80	42	421.43	132.74	15.33	C30W80T42	0.30	0.80	42	3568.71	1337.34	218.29
C12W80T60	0.12	0.80	60	432.93	127.68	20.79	C30W80T60	0.30	0.80	60	3693.83	1717.86	274.73
C12W80T90	0.12	0.80	90	477.01	144.09	24.16	C30W80T90	0.30	0.80	90	3977.55	1876.19	413.19
C12W90T07	0.12	0.90	7	161.77	32.39	9.95	C30W90T07	0.30	0.90	7	1398.98	492.88	153.83
C12W90T14	0.12	0.90	14	260.76	87.47	13.26	C30W90T14	0.30	0.90	14	1768.91	367.05	12.60
C12W90T28	0.12	0.90	28	324.08	110.92	20.17	C30W90T28	0.30	0.90	28	2373.95	816.56	133.62
C12W90T42	0.12	0.90	42	410.78	172.23	19.04	C30W90T42	0.30	0.90	42	2400.32	727.02	73.14
C12W90T60	0.12	0.90	60	429.24	171.31	11.33	C30W90T60	0.30	0.90	60	2842.18	1162.58	251.79
C12W90T90	0.12	0.90	90	469.25	126.67	20.90	C30W90T90	0.30	0.90	90	3283.40	965.46	125.80
C18W50T07	0.18	0.50	7	2469.45	684.58	129.45							

(continued on next page)

– (continued)

Specimen	Cc	Cw	Tc (day)	UCS (kPa)	Tp (kPa)	Tt (kPa)	Specimen	Cc	Cw	Tc (day)	UCS (kPa)	Tp (kPa)	Tt (kPa)
C18W50T14	0.18	0.50	14	2580.66	1504.34	280.70							
C18W50T28	0.18	0.50	28	3431.97	2026.57	480.12							
C18W50T42	0.18	0.50	42	4075.51	2131.92	424.77							
C18W50T60	0.18	0.50	60	4432.27	2152.95	476.92							
C18W50T90	0.18	0.50	90	4931.29	2347.00	475.85							
C18W60T07	0.18	0.60	7	1546.43	498.76	221.36							
C18W60T14	0.18	0.60	14	2085.78	653.60	106.10							
C18W60T28	0.18	0.60	28	2291.43	1174.05	218.56							
C18W60T42	0.18	0.60	42	2548.09	1649.57	140.92							
C18W60T60	0.18	0.60	60	2878.23	1530.54	331.57							
C18W60T90	0.18	0.60	90	3098.16	1691.02	312.63							
C18W70T07	0.18	0.70	7	898.78	294.60	26.16							
C18W70T14	0.18	0.70	14	1157.21	347.57	64.95							
C18W70T28	0.18	0.70	28	1243.20	399.04	83.61							
C18W70T42	0.18	0.70	42	1506.12	491.96	87.54							
C18W70T60	0.18	0.70	60	1802.99	532.03	93.50							
C18W70T90	0.18	0.70	90	1983.95	599.07	63.61							
C18W80T07	0.18	0.80	7	505.65	68.49	19.04							
C18W80T14	0.18	0.80	14	744.76	177.90	14.99							
C18W80T28	0.18	0.80	28	776.53	143.42	19.30							
C18W80T42	0.18	0.80	42	936.05	306.70	91.85							
C18W80T60	0.18	0.80	60	1039.52	323.36	65.05							
C18W80T90	0.18	0.80	90	1142.72	329.27	61.41							
C18W90T07	0.18	0.90	7	421.02	183.89	38.44							
C18W90T14	0.18	0.90	14	586.75	234.27	67.23							
C18W90T28	0.18	0.90	28	763.88	281.17	32.83							
C18W90T42	0.18	0.90	42	863.06	326.27	30.41							
C18W90T60	0.18	0.90	60	969.22	303.74	29.70							
C18W90T90	0.18	0.90	90	1083.40	335.28	48.86							

REFERENCES

[1] Kitazume M, Terashi M. The deep mixing method. London: CRC press; 2013.

[2] Sun J, Wang Y, Liu S, Dehghani A, Xiang X, Wei J, et al. Mechanical, chemical and hydrothermal activation for waste glass reinforced cement. Construct Build Mater 2021;301:124361.

[3] Luo Y, Zheng H, Zhang H, Liu Y. Fatigue reliability evaluation of aging prestressed concrete bridge accounting for stochastic traffic loading and resistance degradation. Adv Struct Eng 2021. 13694332211017995. https://doi.org/10.1177/13694332211017995.

[4] Xu D-s, Huang M, Zhou Y. One-dimensional compression behavior of calcareous sand and marine clay mixtures. Int J GeoMech 2020;20(9):04020137. https://doi.org/10.1061/(ASCE)GM.1943-5622.0001763.

[5] Han J. Principles and practice of ground improvement. 2014 [Principles and Practice of Ground Improvement].

[6] Li J, Qin Q, Sun J, Ma Y, Li Q. Mechanical and conductive performance of electrically conductive cementitious composite using graphite, steel slag, and GGBS. Struct Concr 2020.

[7] Tang Y, Feng W, Chen Z, Nong Y, Guan S, Sun J. Fracture behavior of a sustainable material: recycled concrete with waste crumb rubber subjected to elevated temperatures. J Clean Prod 2021:128553.

[8] Dehghani A, Aslani F, Panah NG. Effects of initial SiO2/Al2O3 molar ratio and slag on fly ash-based ambient cured geopolymer properties. Construct Build Mater 2021;293:123527.

[9] Aslani F, Dehghani A, Wang L. The effect of hollow glass microspheres, carbon nanofibers and activated carbon powder on mechanical and dry shrinkage performance of ultra-lightweight engineered cementitious composites. Construct Build Mater 2021;280:122415.

[10] Aslani F, Deghani A, Asif Z. Development of lightweight rubberized geopolymer concrete by using polystyrene and recycled crumb-rubber aggregates. J Mater Civ Eng 2020;32(2):4019345.

[11] Sun J, Aslani F, Wei J, Wang X. Electromagnetic absorption of copper fiber oriented composite using 3D printing. Construct Build Mater 2021;300:124026.

[12] Cecs147. Technical specification for soil mass with reinforced cement soil pile and anchors. Beijing, China: China Planning Press; 2016.

[13] Zhang C, Gholipour G, Mousavi AA. State-of-the-art review on responses of RC structures subjected to lateral impact loads. Arch Comput Methods Eng 2021;28(4):2477–507. https://doi.org/10.1007/s11831-020-09467-5.

[14] Huang H, Huang M, Zhang W, Yang S. Experimental study of predamaged columns strengthened by HPFL and BSP under combined load cases. Structure and Infrastructure Engineering 2021;17(9):1210–27. https://doi.org/10.1080/15732479.2020.1801768.

[15] Sun L, Li C, Zhang C, Su Z, Chen C. Early monitoring of rebar corrosion evolution based on FBG sensor. Int J Struct Stabil Dynam 2018;18(8):1840001. https://doi.org/10.1142/S0219455418400011.

[16] Chen C, Zhang G, Zornberg JG, Morsy AM, Zhu S, Zhao H. Interface behavior of tensioned bars embedded in cement-soil mixtures. Construct Build Mater 2018;186:840–53.

[17] Chen FX, Zhong YC, Gao XY, Jin ZQ, Wang ED, Zhu FP, et al. Non-uniform model of relationship between surface strain

and rust expansion force of reinforced concrete. Sci Rep 2021;11(1):1–9. https://doi.org/10.21203/rs.3.rs-135397/v1.
[18] Chen F, Jin Z, Wang E, Wang L, Jiang Y, Guo P, et al. Relationship model between surface strain of concrete and expansion force of reinforcement rust. Sci Rep 2021;11(1):1–11. https://doi.org/10.1038/s41598-021-83376-w.
[19] Ou Y, Zhu D, Zhang H, Huang L, Yao Y, Li G, et al. Mechanical characterization of the tensile properties of glass fiber and its reinforced polymer (GFRP) composite under varying strain rates and temperatures. Polymers 2016;8(5):196.
[20] Wang H, Sun X, Peng G, Luo Y, Ying Q. Experimental study on bond behaviour between BFRP bar and engineered cementitious composite. Construct Build Mater 2015;95:448–56.
[21] Zhang W, Tang Z. Numerical modeling of response of CFRP–concrete interfaces subjected to fatigue loading. J Compos Construct 2021;25(5):04021043. https://doi.org/10.1061/(ASCE)CC.1943-5614.0001154.
[22] Xu D, Liu Q, Qin Y, Chen B. Analytical approach for crack identification of glass fiber reinforced polymer–sea sand concrete composite structures based on strain dissipations. Struct Health Monit 2020. https://doi.org/10.1177/1475921720974290. 1475921720974290.
[23] Aslani F, Gunawardena Y, Dehghani A. Behaviour of concrete filled glass fibre-reinforced polymer tubes under static and flexural fatigue loading. Construct Build Mater 2019;212:57–76.
[24] Ju Y, Shen T, Wang D. Bonding behavior between reactive powder concrete and normal strength concrete. Construct Build Mater 2020;242:118024. https://doi.org/10.1016/j.conbuildmat.2020.118024.
[25] Zhang W, Tang Z, Yang Y, Wei J, Stanislav P. Mixed-mode debonding behavior between CFRP plates and concrete under fatigue loading. J Struct Eng 2021;147(5):4021055. https://doi.org/10.1061/(ASCE)ST.1943-541X.0003032.
[26] Li X, Yang H, Zhang J, Qian G, Yu H, Cai J. Time-domain analysis of tamper displacement during dynamic compaction based on automatic control. Coatings 2021;11(9):1092. https://doi.org/10.3390/coatings11091092.
[27] Timoney MJ, McCabe BA. Strength verification of stabilised soil-cement columns: a laboratory investigation of the push-in resistance test (PIRT). Canadian Geotech J 2017;54(6):789–805.
[28] Xu J, Wu Z, Chen H, Shao L, Zhou X, Wang S. Study on strength behavior of basalt fiber-reinforced loess by digital image technology (DIT) and scanning Electron microscope (SEM). Arabian J Sci Eng 2021:1–20. https://doi.org/10.1007/s13369-021-05787-1.
[29] Wu C, Wang X, Chen M, Kim J M. Differential received signal strength based RFID positioning for construction equipment tracking. Adv Eng Inf 2019;42:100960.
[30] Åhnberg H. Strength of stabilised soil - a laboratory study on clays and organic soils stabilised with different. Types of Binder 2006;87(1):35–40.
[31] Timoney MJ, McCabe BA, Bell AL. Experiences of dry soil mixing in highly organic soils. Proceedings of the Institution of Civil Engineers-Ground Improvement 2012;165(1):3–14.
[32] Zhu J, Chen Y, Zhang L, Guo B, Fan G, Guan X, et al. Revealing the doping mechanism of barium in sulfoaluminate cement clinker phases. J Clean Prod 2021;295:126405. https://doi.org/10.1016/j.jclepro.2021.126405.
[33] Dantas ATA, Batista Leite M, de Jesus Nagahama K. Prediction of compressive strength of concrete containing construction and demolition waste using artificial neural networks. Construct Build Mater 2013;38:717–22. https://doi.org/10.1016/j.conbuildmat.2012.09.026.
[34] Wang L, Yuan J, Wu C, Wang X. Practical algorithm for stochastic optimal control problem about microbial fermentation in batch culture. Optimisation Letters 2019;13(3):527–41.
[35] Feng W, Wang Y, Sun J, Tang Y, Wu D, Jiang Z, et al. Prediction of thermo-mechanical properties of rubber-modified recycled aggregate concrete. Construct Build Mater 2022;318:125970.
[36] Sun J, Wang X, Zhang J, Xiao F, Sun Y, Ren Z, et al. Multi-objective optimisation of a graphite-slag conductive composite applying a BAS-SVR based model. J Build Eng 2021;44:103223.
[37] Zhang J, Sun Y, Li G, Wang Y, Sun J, Li J. Machine-learning-assisted shear strength prediction of reinforced concrete beams with and without stirrups. Eng Comput 2020:1–15.
[38] Sun Y, Li G, Zhang J, Sun J, Xu J. Development of an ensemble intelligent model for assessing the strength of cemented paste backfill. Adv Civ Eng 2020:2020. https://doi.org/10.1155/2020/1643529.
[39] Sun J, Wang Y, Yao X, Ren Z, Zhang G, Zhang C, et al. Machine-learning-Aided prediction of flexural strength and ASR expansion for waste glass cementitious composite. Appl Sci 2021;11(15):6686.
[40] Liu J, Wu C, Wu G, Wang X. A novel differential search algorithm and applications for structure design. Appl Math Comput 2015;268:246–69.
[41] Xu S, Wang J, Shou W, Ngo T, Sadick M A, Wang X. Computer vision techniques in construction: a critical review. Arch Comput Methods Eng 2021;28(5):3383–97. https://doi.org/10.1007/s11831-020-09504-3.
[42] Zhou Z-H. Ensemble methods: foundations and algorithms. CRC Press; 2012.
[43] Abedini M, Zhang C. Dynamic performance of concrete columns retrofitted with FRP using segment pressure technique. Compos Struct 2021;260:113473. https://doi.org/10.1016/j.compstruct.2020.113473.
[44] Chou J-S, Ngo N-T, Pham A-D. Shear strength prediction in reinforced concrete deep beams using nature-inspired metaheuristic support vector regression. J Comput Civ Eng 2016;30(1):4015002.
[45] Du Y, Pan N, Xu Z, Deng F, Shen Y, Kang H. Pavement distress detection and classification based on YOLO network. Int J Pavement Eng 2020:1–14. https://doi.org/10.1080/10298436.2020.1714047.
[46] Sun J, Ma Y, Li J, Zhang J, Ren Z, Wang X. Machine learning-aided design and prediction of cementitious composites containing graphite and slag powder. J Build Eng 2021:102544.
[47] Zhang J, Huang Y, Ma G, Nener B. Multi-objective beetle antennae search algorithm. arXiv preprint arXiv:2002.10090 2020.
[48] Zhang J, Huang Y, Wang Y, Ma G. Multi-objective optimisation of concrete mixture proportions using machine learning and metaheuristic algorithms. Construct Build Mater 2020;253:119208.
[49] Gb175. Common Portland cement. 2007. 03.
[50] Chen C, Zhang G, Zornberg G J, Morsy M A, Huang J. Interface bond behavior of tensioned glass fiber-reinforced polymer (GFRP) tendons embedded in cemented soils. Construct Build Mater 2020;263:120132.
[51] Teng Y, Zhang YJ, Yan ML, Zhang F, Zhang DG, Yuan NZ. Technical code for ground treatment of buildings. Beijing: China Architecture & Building Press; 2012.
[52] Singh V, Gu N, Wang X. A theoretical framework of a BIM-based multi-disciplinary collaboration platform. Autom ConStruct 2011;20(2):134–44.

[53] Chen C, Liang G, Liu X, Tang Y, Xu Y, Liu J, et al. A device and method for preparing soil samples used in testing frictional performance of anchor/pile-soil interface. China Patent ZL 2014;1:176979. 8.
[54] Chen C, Zhang G, Zornberg G J, Zheng X. Element nail pullout tests for prediction of soil nail pullout resistance in expansive clays. Geotech Test J 2019;42(5):1274–97.
[55] Schapire RE. The boosting approach to machine learning: an overview. In: Nonlinear estimation and classification. Springer; 2003. p. 149–71.
[56] Breiman L. Bagging predictors. Mach Learn 1996;24(2):123–40. https://doi.org/10.1007/BF00058655.
[57] Yang X-S. Firefly algorithms for multimodal optimisation. In: International symposium on stochastic algorithms. Springer; 2009.
[58] Hsu W C, Chang C C, Lin J C. A practical guide to support vector classification. National Taiwan University; 2003.
[59] Xiujuan L, Zhongke S. Overview of multi-objective optimisation methods. J Syst Eng Electron 2004;15(2):142–6.
[60] Yang X-S. Bat algorithm for multi-objective optimisation. Int J Bio-Inspired Comput 2011;3(5):267–74.
[61] Baykasoğlu A, Öztaş A, Özbay E. Prediction and multi-objective optimisation of high-strength concrete parameters via soft computing approaches. Expert Syst Appl 2009;36(3):6145–55.
[62] Yoon KP, Hwang C-L. Multiple attribute decision making: an introduction. Sage publications; 1995.
[63] Cortez P, Embrechts MJ. Using sensitivity analysis and visualization techniques to open black box data mining models. Inf Sci 2013;225:1–17.